ACS APPLIED POLYMER MATERIALS

pubs.acs.org/acsapm Letter

Surface Mechanical Behavior of Water-Spread Poly(styrene)−Poly(ethylene glycol) Cylindrical Micelles at the Air−Water Interface

Taesuk Jun, Daniel J. Fesenmeier, and You-Yeon Won*

Cite This: ACS Appl. Polym. Mater. 2024, 6, 2054−2060 Read Online

ACCESS | Metrics & More | Article Recommendations | Supporting Information

ABSTRACT: We investigated the air−water interfacial properties of poly(styrene)−poly(ethylene glycol) (PS−PEG) micelles for potential use in treating respiratory distress syndrome (RDS). We created kinetically frozen cylindrical PS−PEG micelles through equilibration−nanoprecipitation. Similar to spherical micelles, cylindrical micelles generated high surface pressure during compression, a crucial factor for the RDS treatment. However, cylindrical micelles displayed a unique monolayer-to-bilayer transition, resulting in an additional plateau in their surface pressure−area isotherm before eventual collapse during compression, a phenomenon absent in spherical micelles. Moreover, cylindrical micelles exhibited an increased isotherm hysteresis during compression−expansion cycles. These distinct characteristics have the potential to make cylindrical nanostructures more advantageous for the intended applications.

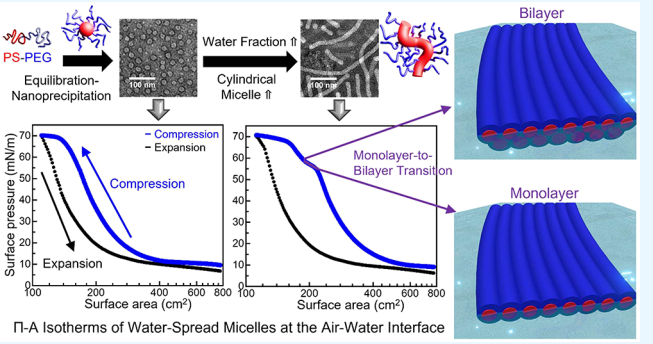

KEYWORDS: *Amphiphilic block copolymer micelle, micelle shape, cylindrical micelles, surface pressure−area isotherm, poly(styrene)−poly(ethylene glycol)*

The alveolar surface of the lungs is protected by lung surfactant (LS), and its deficiency can lead to serious respiratory disorders.[1,2] One such disorder is neonatal respiratory distress syndrome (NRDS), which predominantly affects premature infants, resulting in breathing complications, reduced lung compliance, and alveolar collapse.[3] Another critical respiratory ailment is acute respiratory distress syndrome (ARDS), marked by hypoxemia and diminished respiratory compliance, posing a life-threatening scenario.[4] The recent SARS-CoV-2 (COVID-19) pandemic has significantly escalated ARDS instances, with reports indicating that over 15% of severely ill COVID-19 patients develop ARDS.[5] Clinical therapies involving exogenous LS administration are currently addressing lung dysfunction in NRDS. However, in ARDS, challenges arise from LS deactivation due to inflammation and contamination with plasma/blood proteins.[6]

In the quest for a potent LS therapy for ARDS, substantial headway has been made in developing polymer lung surfactant (PLS).[4] PLS distinguishes itself by avoiding disruption caused by protein-rich exudate and inflammation, making it a promising therapy for respiratory disorders, particularly ARDS.[7,8] Our prior research efforts have highlighted the suitability of poly(styrene)-*block*-poly(ethylene glycol) (PS−PEG) for applications in PLS.[4,7] PS−PEG micelles exhibit high surface pressure ($\Pi > 60$ mN/m) and reliable respreading at the air−water interface during repeated compression and expansion cycles, satisfying the Laplace stability criterion.[9] The efficacy of PS−PEG micelles in mitigating lung dysfunction was effectively demonstrated through successful *in vivo* experiments.[8,10] These positive results have prompted further investigations into the fundamental properties governing the air−water interface behavior of PS−PEG micelle systems.[11−13]

To optimize the effectiveness of PLS therapy, it might be beneficial to fine-tune PLS to emulate the phase transition behaviors observed in lipid Langmuir films at the air−water interface, ensuring a metastable state at elevated surface pressure levels.[14] In terms of the surface pressure−area (Π−A) isotherm behavior, the majority of exogenous LSs undergo these phase transitions, maintaining an equilibrium surface pressure (Π_e) at 40−50 mN/m.[14] Atomic force microscopy (AFM) images revealed the presence of multilayer domains developing in an island-like shape during the phase transition processes.[15] This establishes a remarkable state of metastability

Received: January 12, 2024
Revised: January 24, 2024
Accepted: January 31, 2024
Published: February 9, 2024

https://doi.org/10.1021/acsapm.4c00109
ACS Appl. Polym. Mater. 2024, 6, 2054−2060

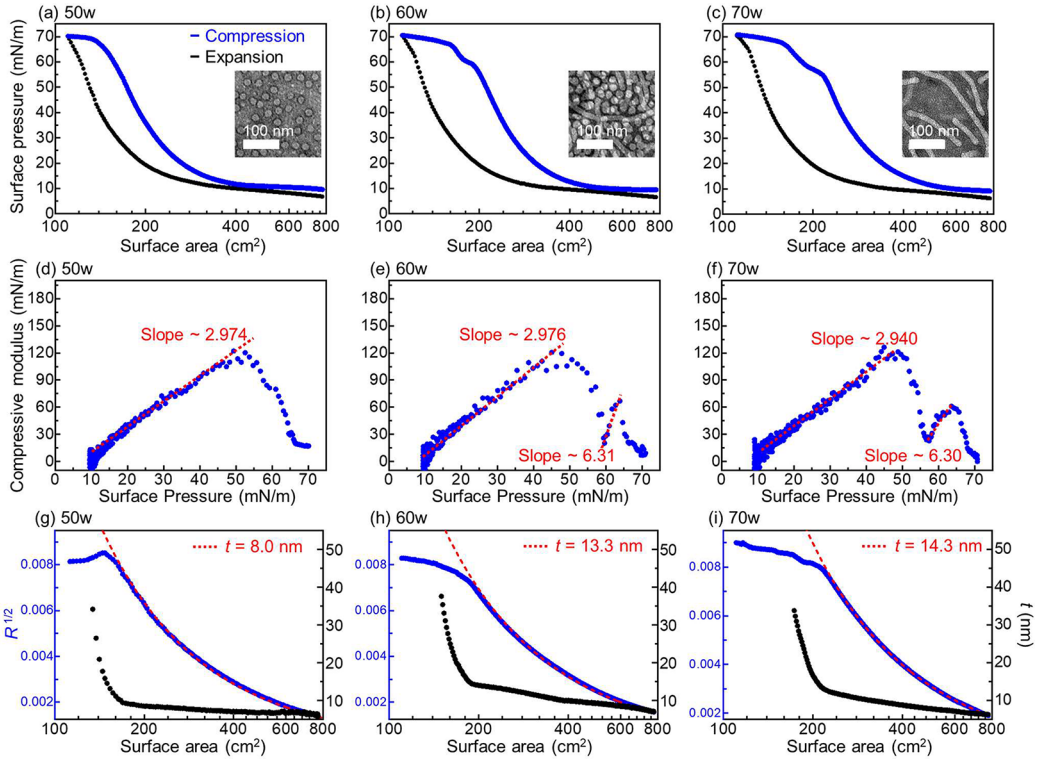

Figure 1. (a–c) Π–*A* isotherms of PS–PEG micelles (300 μL of 5 mg/mL solution) for the (a) 50w, (b) 60w, and (c) 70w samples compressed at a rate of 30 mm/min at 25 °C. (d–f) Compressive modulus ($E = -A\frac{d\Pi}{dA}$) plots as a function of surface pressure for the (d) 50w, (e) 60w, and (f) 70w samples. (g–i) Plots of square root of reflectivity ($R^{1/2}$, depicted in blue) alongside the estimated optical thickness (*t*, represented in black) for the (g) 50w, (h) 60w, and (i) 70w samples. The excellent quality of the constant-thickness fits for the reflectivity data of the 60w and 70w samples (indicated by the red dotted curves in (h) and (i), respectively) highlights that the minor gradual increases in thickness values derived from the constant-mass fits of these data sets (represented by the black data points in (h) and (i), respectively) are likely statistically insignificant.

($\Pi_{max} > \Pi_e$), believed to be a safeguard against alveolar collapse at elevated Π.[16]

The surface micelles, forming a monolayer through block copolymer spreading using an organic cosolvent, have demonstrated surface phase transition behaviors with various micellar morphologies.[17] Consequently, engineering PLS with micellar morphologies inducing a phase transition during compression might offer therapeutic benefits, akin to natural lipid-based lung surfactants.

The micellar morphology of the block copolymer can be controlled by factors such as chemical composition of repeating units, solvent choice, and solvent-to-nonsolvent ratio.[18] Notably, the solvent-to-nonsolvent ratio has been proposed as a method for precisely controlling micelle morphology due to its ease of implementation.[19] Despite numerous studies on cylindrical surface micelles, the realm of water-spread cylindrical micelles remains largely unexplored in the existing literature. This study focuses on the influence of micelle morphology, particularly the cylindrical configuration, on the surface mechanical behavior of water-spread PLS polymer micelles. Our approach entails control over the shape of self-assembled kinetically frozen micelles in the prespreading stage through distinct conditions within the equilibration–nanoprecipitation (ENP) process; the key factor influencing micelle morphology was identified as the solvent composition, specifically the water content.[20]

Micelle formation was achieved using the PS–PEG (M_n = 5.2 and 5.5 kDa, respectively) block copolymer through the ENP process.[21] Our prior research indicated that when the initial water/acetone mixture possessed a water fraction of ≤ 60 vol % during the ENP process at room temperature, PS–PEG micelles exhibited predominantly spherical morphologies.[21] Within this water fraction range, we noted that an increase in the water fraction resulted in a significant increase in the micelle size (aggregation number). This phenomenon is attributed to the escalating incompatibility between PS and the solvent mixture, aligning with predictions derived from micelle theory.[22] Beyond a water fraction of 60 vol %, the micelles adopted a cylindrical shape until reaching ~ 80 vol %, at which point the PS–PEG polymer lost its dispersibility and underwent precipitation (unpublished results).

For this reason, in the current study, micelles were prepared using three distinct water/acetone mixtures with water fractions of 50, 60, and 70 vol % during the ENP process, denoted as 50w, 60w, and 70w, respectively. Dynamic light scattering (DLS) was employed to determine their hydrodynamic diameters (D_h) and polydispersity indices (PDI). The DLS results (Figure S1) revealed distinct characteristics across the micelle samples. The 50w micelles displayed a unimodal shape in their particle size distribution. In contrast, the 60w and 70w micelles demonstrated bimodal shapes. The increased-diameter peaks in the particle distributions for the 60w and 70w samples compared to the 50w sample suggest the existence of separate micelle types, specifically cylindrical micelles. Moreover, the 70w sample exhibited a larger area fraction for the increased-diameter peak (79.2%) than the 60w sample (55.4%) (Table S1).

https://doi.org/10.1021/acsapm.4c00109
ACS Appl. Polym. Mater. 2024, 6, 2054–2060

It should be noted that in our prior studies,[12,21] we consistently observed the dominance of spherical micelles at the 60 vol % water fraction ENP condition. However, both the current investigation and our latest study have revealed the formation of elongated cylindrical micelles under the same 60 vol % water fraction condition. Although the exact cause of this discrepancy remains elusive, we suspect that it stems from the 60 vol % water fraction serving as the precise boundary between spherical and cylindrical morphologies. Minor fluctuations in experimental conditions, such as variations in the water content and temperature, likely contribute to the observed divergence in micelle shapes. Supplementary experiments were conducted to explore this possibility further. Figure S2 and Table S2 demonstrate that a slight decrease in ENP water composition (from 60 to 57 vol %) or a slight rise in room temperature during the ENP process (from 20 to 25 °C) induced a transition from predominantly cylindrical to predominantly spherical micelles. Notably, variations in the agitation speed during ENP did not yield any significant changes in the micelle morphology. These results suggest that seasonal fluctuations in laboratory room temperature may have contributed to the observed inconsistency, as all ENP processes were conducted at room temperature without precise temperature control. Unfortunately, specific temperature values were not recorded during our experiments. However, this aspect does not affect the main conclusion of the present investigation.

Transmission electron microscopy (TEM) images (Figures 1a−c and S3a−c) displayed well-defined spherical micelles for the 50w sample, a combination of spherical and cylindrical micelles for the 60w sample, and a prevalence of cylindrical micelles for the 70w sample. In terms of quantitative analysis, the core diameters of polymer micelles (D_c) were estimated through TEM measurements. These measurements revealed a gradual increase in core diameters, measuring 19.3, 21.1, and 22.6 nm for the 50w, 60w, and 70w samples, respectively, indicating an increase in micellar aggregation with higher water fractions during the ENP process, leading to a transition from spherical to cylindrical micelles (Table S1).

The Π−A isotherms for the 50w, 60w, and 70w samples are depicted in Figure 1a−c. At surface areas below approximately 288, 350, and 400 cm^2 for the 50w, 60w, and 70w samples, respectively, the surface pressure exhibited equilibrium Π values similar to those of adsorbed PEG films ($\Pi_{e,PEG} \cong 10$ mN/m).[23] This observation implies that in this regime, the areas per micelle for all the samples lie below their hydrodynamic areas (Figure S4), indicating osmotic pressure accumulation within a three-dimensional (3D) PEG sublayer; this osmotic pressure buildup arises from the overlap between the PEG corona layers of neighboring micelles in the subphase region.[13]

The surface pressure of the 50w sample exhibited continued growth to 70 mN/m. In contrast, the 60w and 70w samples reached plateaus at approximately 60 and 55 mN/m, respectively. This plateau phenomenon at Π > 40 mN/m during compression is a known trait shared by lipid-based replacement surfactants like Survanta, Curosurf, and Infasurf.[24] This plateau Π_e region signifies the transition from monolayer to multilayer structure, as established through AFM observations of film structures. As will be explained in detail later, the emergence of high plateau Π_e for the 60w and 70w samples is governed by a shared underlying mechanism, namely, the monolayer-to-bilayer transition specific to cylindrical micelles.

The compressive modulus ($E = -A\frac{d\Pi}{dA}$) plots (Figure 1d−f) exhibited a linear correlation between the modulus and surface pressure above $\Pi_{e,PEG}$ (∼ 10 mN/m) for all samples. From de Genne's osmotic pressure scaling theory applicable to semidilute solutions,[25] the following relationship emerges: $E = y\Pi$, with the coefficient $y = dv/(dv - 1)$, where d and v represent the dimensionality and Flory exponent, respectively. For a 3D scenario ($d = 3$), the modulus plots within Π = 10−45 mN/m yielded v values of approximately 0.502 to 0.519 across all the samples. Importantly, these values closely agree with the previously reported Flory exponent of around 0.50 for PEG in a water environment.[26]

During the compression beyond the secondary plateau, we observed sharp escalations in the modulus where the slopes amount to 6.07 and 6.30 for the 60w and 70w samples, respectively, signifying a resurgence of incompressibility. These observed values agree with estimations derived from the reported compressibility behavior of PS nanoparticles at the air−water interface, as documented in Kumaki's research.[27] This implies a potential link to the origin of elasticity within the PS−PEG cylindrical micelle multilayers: the mechanical resistance of these multilayers against compression likely stems from cohesive bonding between micelles, analogous to the bonding between PS nanoparticles at the same air−water interface. While intriguing, a more comprehensive investigation is warranted to fully grasp the nuances of this analogy.

Quantitative Brewster angle microscopy (QBAM) was employed to measure the reflectivity (R) of the water-spread micelles film at the Brewster angle, correlating with the optical thickness of the micelle film. The dependence of R on the optical thickness of the film (t) and the refractive index of the micelle film (n_f) is expressed through eq 1:

$$R^{1/2} = \frac{\pi t}{\lambda} \cdot \frac{n_f^{\,2} - n_w^{\,2} - 1 + (n_w/n_f)^2}{(1 + n_w^{\,2})^{1/2}} \quad (1)$$

where λ denotes the incident wavelength (658 nm) and n_w stands for the refractive index of water.[28] Furthermore, n_f can be estimated using eq 2:

$$n_f = n_w + \frac{dn}{dc} \cdot \frac{M}{At} \quad (2)$$

where M is the total mass of micelles at the air−water interface and $\frac{dn}{dc}$ is the refractive index increment of the micelle film. In the context of insoluble films featuring rigid core domains, a relatively constant mass M is expected during the compression process. Figure 1g−i depicts plots of the square root of the reflectivity ($R^{1/2}$) (blue lines) alongside fits of estimated optical thickness for the micelle films (black symbols) in relation to A at 25 °C. Reflectivity data within initial range of A (770 to 240 cm^2) agree with constant thickness models (red dashed lines) corresponding to t values of 8.0, 13.3, and 14.3 nm for the 50w, 60w, and 70w samples, respectively. Notably, this thickness, approximately half of the micelle core diameter, suggests submersion of micelle cores in water within film interstitial regions at an early stage of compression.

A previous study found that the optical film thickness sharply increases when the monolayer transitions into collapse or wrinkle structure.[29] In the 50w sample, this elevation in t corresponded to the initiation of micelle film collapse at a specific Π of 61.6 mN/m and a corresponding A of 153.7 cm^2. For the 60w and 70w samples, the rise in t took place at Π

https://doi.org/10.1021/acsapm.4c00109
ACS Appl. Polym. Mater. 2024, 6, 2054−2060

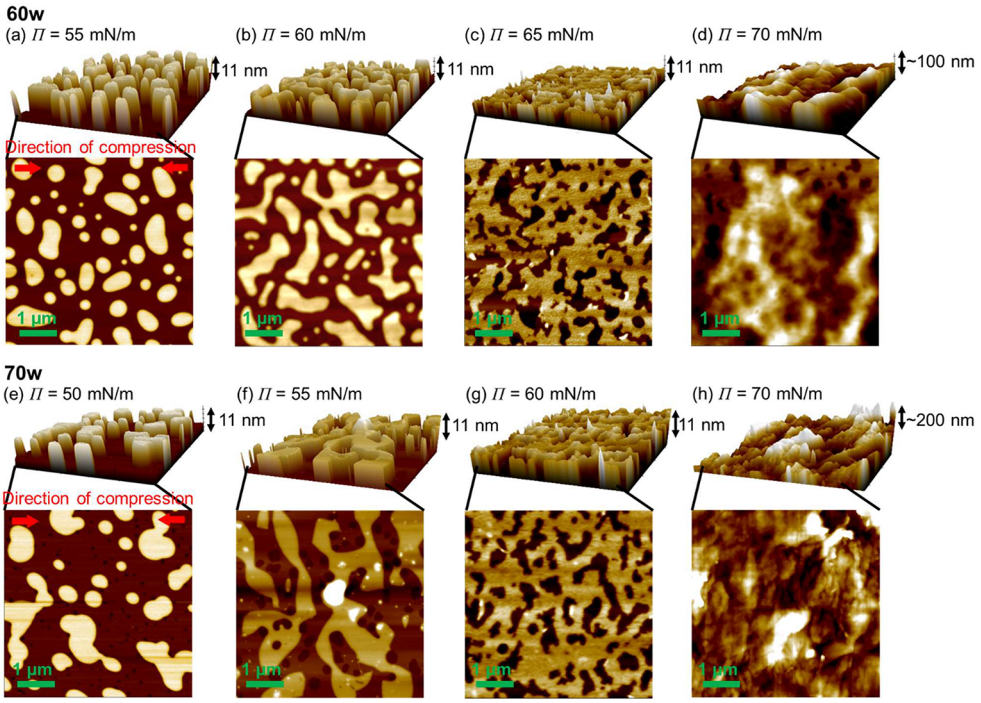

Figure 2. Lateral structures and AFM images of the (a–d) 60w and (e–h) 70w films under constant surface pressure near Π_e at 25 °C. The films were transferred by the Langmuir–Blodgett method while maintaining controlled surface pressure. All AFM images have a scanning area of 5 μm × 5 μm. The top rows of each AFM image show 3D renderings with a typical z range.

values of 58.4 and 54.9 mN/m and corresponding A values of 192.5 and 216.4 cm^2, respectively, prior to the ultimate collapse regime. Importantly, this increase in thickness aligned with the transition of micelle films from a monolayer to a bilayer configuration, occurring at $\Pi_e \cong 60$ and 55 mN/m for the 60w and 70w samples, respectively. Furthermore, BAM images for the 60w and 70w samples reveal the absence of wrinkle structures even at high Π (Figure S5). This absence is likely attributed to the configuration of bilayers rather than wrinkle structures, in stark contrast to the 50w sample, which exhibited wrinkle formation at $\Pi \cong 70$ mN/m before undergoing mechanical collapse (Figure S5; also see ref 21). Consequently, spherical and cylindrical monolayers exhibit entirely distinct mechanical responses to compression. This represents a complex question that warrants further extensive investigation in the future.

Topological morphologies of micelle films during compression were estimated by AFM imaging. The AFM phase image of PS–PEG dewetted on a mica substrate displayed a significant contrast of ∼ 40° between the covered and uncovered regions (Figure S6). At low Π (10 mN/m, Figures S7–S9), AFM images of all samples exhibited dark minority domains (holes) with a height difference (h) of approximately 3 nm, yet phase images showed a consistent 4° phase difference for all PS–PEG micelle films, suggesting effective coverage of the air–water interface. The presence of these approximately 3 nm deep holes is likely an artifact generated during the Langmuir–Blodgett transfer process, suggesting reduced monolayer stability at Π < 30 mN/m as documented in lipid films.[30] The precise mechanism responsible for the formation of these holes remains unknown but falls outside the scope of our current study. Upon increasing Π, the area and number of dark regions decreased for all of the samples. For the 60w and 70w samples (Figures S8b and S9b), island-like white regions ($h \cong 11$ nm) appeared. This h corresponds to about half of the micelle core diameter estimated from TEM, indicating the formation of a stacked bilayer structure in the micelle film. AFM phase images (Figure S10) unveiled a minimal 4° phase difference between the monolayer and bilayer, suggesting consistent film coverage with different polymer layering. Notably, the 50w sample lacked such island-like white regions at Π = 30 mN/m (Figure S7b). Instead, irregular dotlike shapes emerged at Π = 50 mN/m, indicating the ejection of spherical micelles pushed upward from the monolayer film (Figure S7c).

Figure 2 displays AFM images captured near Π_e (60 and 55 mN/m for the 60w and 70w samples, respectively). With a slight increase in Π, there is continuous expansion in the island (or bilayer) area, indicating the transition of monolayers into bilayers within the range of Π_e values. Following this phase transition, further compression of the 60w and 70w films leads to the emergence of area-spanning (percolated) multilayer domains, as illustrated in Figure 2c,g. This transformation effectively converts the micelle films to a fully elastic state, consequently contributing to the observed upturn in surface pressure in this regime, as depicted in Figure 1b,c. Subsequently, the films enter the collapse regime, resulting in significant height fluctuations characterized by height differences exceeding 100 and 200 nm for the 60w and 70w samples, respectively (Figure 2d,h). Despite the horizontal application of compression (indicated by the red arrow), both bilayer formation and film collapse yield randomly oriented patterns similar to those observed in multilayer domains of other lipid-based exogenous LS studies.[15] In all AFM images of the 60w and 70w samples, we did not observe the alignment of cylindrical micelles, nor were we able to visualize individual micelle strands. A more detailed characterization of micelle

https://doi.org/10.1021/acsapm.4c00109
ACS Appl. Polym. Mater. 2024, 6, 2054–2060

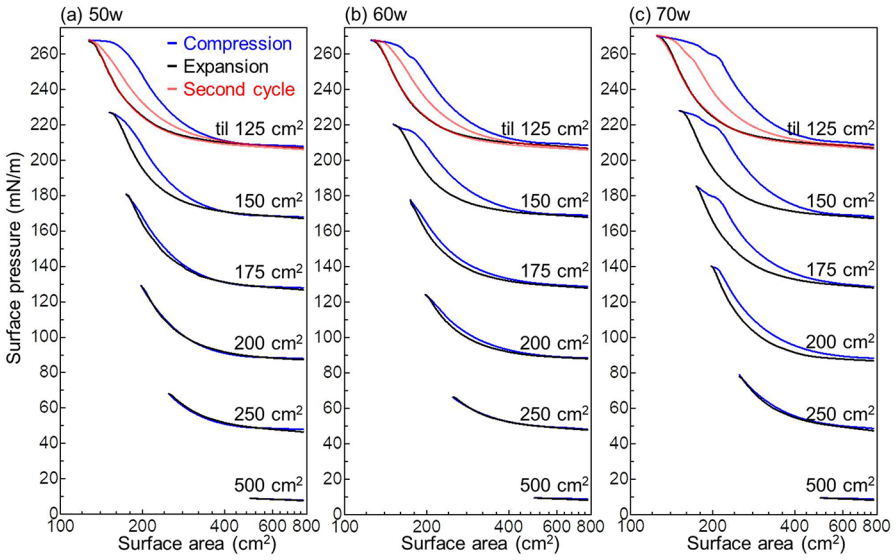

Figure 3. Π−*A* isotherms for the (a) 50w, (b) 60w, and (c) 70w films at 25 °C, starting from an initial area of 777 cm^2 and compressing to various final areas of 500, 250, 200, 175, 150, and 125 cm^2 with a uniform barrier position rate of 30 mm/min. Each Π−*A* isotherm is vertically shifted by 30 mN/m for clarity.

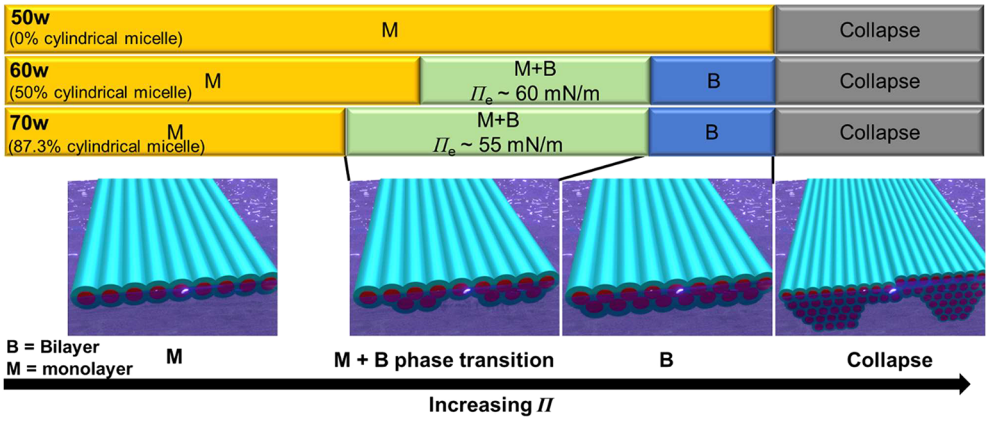

Figure 4. Schematic illustration of the surface mechanical behaviors of water-spread PS−PEG micelles at the air−water interface, featuring different fractions of cylindrical shapes (50w, 60w, and 70w) during compression.

orientations seems to necessitate the use of other techniques such as grazing incidence X-ray scattering methods.

Hysteresis, a common feature in lung surfactant films, is distinguished by differences in the Π−*A* isotherms between the compression and expansion cycles. To investigate the hysteresis behavior in our system, we systematically adjusted the final compression area during each cyclic Π−*A* isotherm measurement. Figure 3 presents the Π−*A* isotherms of the 50w, 60w, and 70w samples at 25 °C, starting from an initial surface area of 777 cm^2 and compressing to various final areas (500, 250, 200, 175, 150, and 125 cm^2) with a constant barrier position rate of 30 mm/min. When compression is halted before the monolayer-to-bilayer phase transition, there is a slight difference in the Π−*A* isotherms between the compression and expansion cycles for both the 60w and 70w samples. However, when dynamic compression reaches final surface areas within the phase transition region, the hysteresis between compression and expansion begins to rise. This increase suggests the ejection of micelles from the film during the phase transition.

Hysteresis analysis was performed on the initial compression−expansion cycle with a final compression area of 125 cm^2 for the 50w, 60w, and 70w samples. The normalized hysteresis area (HA_n) is calculated by using the formula $HA_n = HA/(A_{LO} - A_F)$, where HA is the absolute hysteresis, A_{LO} is the lift-off area, and A_F is the final compression area.[21] The results are summarized in Table S3. The respreading ratio, as defined in ref 21, is affected by several factors, one of which is the ability of molecules to be respread at the interface after compression. It is essential to consider that there are unique behaviors associated with the micellar shape. Specifically, the 50w sample undergoes the collapse regime directly from the monolayer, while the 60w and 70w samples go through bilayer formation before entering the collapse regime. This bilayer formation of the cylindrical micelles might act as a reservoir of micelles after compression, resulting in an increased respreading ratio of 60w and 70w (0.459 and 0.366, respectively) compared to that of 50w (0.154).[16]

It is noteworthy that the 70w sample exhibits a larger normalized hysteresis area (21.6 mN/m) than the 60w sample (16.4 mN/m), indicating a slower recovery of the out-of-plane

https://doi.org/10.1021/acsapm.4c00109
ACS Appl. Polym. Mater. 2024, 6, 2054−2060

structures for a higher content of cylindrical micelles. This trend aligns with the respreading ratio, where the respreading ratio for the 70w sample (0.366) is lower than that for the 60w sample (0.459), suggesting that the number of micelles expelled from the film increased for 70w compared to 60w. This observation is further supported by AFM height differences of ∼ 100 and ∼ 200 nm for the 60w and 70w samples, respectively, at the collapse regime of 70 mN/m (Figures 2d,h). Therefore, by quantifying the presence of cylindrical micelles, we can exert control over the respreading behavior, which serves as a pivotal parameter in defining the properties of lung surfactants.

The surface mechanical behaviors of PS−PEG films, influenced by the content of the micelle shapes (spheres and cylinders), are elucidated in Figure 4. In the 50w sample, characterized by spherical micelles, a PS−PEG film exhibits typical monolayer surfactant properties. This behavior resembles that of dipalmitoylphosphatidylcholine (DPPC), which can sustain high surface pressures of up to 70 mN/m. Conversely, in the 60w and 70w samples, where cylindrical micelles coexist with spherical micelles, a phase transition occurs before the onset of the collapse regime. This results in a nearly plateaued Π_e of approximately 60 and 55 mN/m for the 60w and 70w samples, respectively, during compression. This intriguing phase transition behavior has also been reported in other exogenous LS such as Survanta, Curosurf, and Infasurf with $\Pi_e \sim 45$ mN/m.[24] The monolayer-to-bilayer transition from AFM analysis for the 60w and 70w samples ensures a remarkable state of metastability ($\Pi_{max} > \Pi_e$), believed to be a safeguard against alveolar collapse at elevated Π. These findings illustrate the potential for the precise adjustment of the surface mechanical behavior of PLS formulations through the customization of their micellar morphology.

■ ASSOCIATED CONTENT

Supporting Information

The Supporting Information is available free of charge at https://pubs.acs.org/doi/10.1021/acsapm.4c00109.

Experimental procedures, DLS size histograms, representative TEM images, surface pressure−area per micelle isotherms, representative BAM images, supplementary AFM images, and tables summarizing micelle size characteristics (PDF)

■ AUTHOR INFORMATION

Corresponding Author

You-Yeon Won − *Davidson School of Chemical Engineering, Purdue University, West Lafayette, Indiana 47907, United States; Purdue University Institute for Cancer Research, West Lafayette, Indiana 47907, United States;* orcid.org/0000-0002-8347-6375; Email: yywon@purdue.edu

Authors

Taesuk Jun − *Davidson School of Chemical Engineering, Purdue University, West Lafayette, Indiana 47907, United States*

Daniel J. Fesenmeier − *Davidson School of Chemical Engineering, Purdue University, West Lafayette, Indiana 47907, United States*

Complete contact information is available at: https://pubs.acs.org/10.1021/acsapm.4c00109

Notes

The authors declare no competing financial interest.

■ ACKNOWLEDGMENTS

The authors are grateful for funding from NSF (CBET-2211843). The authors also acknowledge support from the Purdue University Institute for Cancer Research (PICR) via an NIH NCI grant (P30 CA023168), which supports the campus-wide NMR shared resources that were utilized in this work. The authors also express their gratitude to Prof. Stephen Beaudoin in the Davidson School of Chemical Engineering at Purdue University for granting them access to his AFM facility.

■ REFERENCES

(1) Weibel, E. R.; Gil, J. Electron microscopic demonstration of an extracellular duplex lining layer of alveoli. *Respir. Physiol.* **1968**, *4* (1), 42−57.

(2) Notter, R. H. *Lung Surfactants: Basic Science and Clinical Applications*; CRC Press, 2000.

(3) Dyer, J. Neonatal Respiratory Distress Syndrome: Tackling A Worldwide Problem. *Pharm. Ther.* **2019**, *44* (1), 12−14.

(4) Kim, H. C.; Won, Y. Y. Clinical, technological, and economic issues associated with developing new lung surfactant therapeutics. *Biotechnology advances* **2018**, *36* (4), 1185−1193.

(5) Schousboe, P.; Ronit, A.; Nielsen, H. B.; Benfield, T.; Wiese, L.; Scoutaris, N.; Verder, H.; Berg, R. M. G.; Verder, P.; Plovsing, R. R. Reduced levels of pulmonary surfactant in COVID-19 ARDS. *Sci. Rep.* **2022**, *12* (1), 4040.

(6) Dushianthan, A.; Cusack, R.; Goss, V.; Postle, A. D.; Grocott, M. P. W. Clinical review: Exogenous surfactant therapy for acute lung injury/acute respiratory distress syndrome - where do we go from here? *Crit. Care* **2012**, *16* (6), 238.

(7) Kim, H. C.; Suresh, M. V.; Singh, V. V.; Arick, D. Q.; Machado-Aranda, D. A.; Raghavendran, K.; Won, Y.-Y. Polymer Lung Surfactants. *ACS Appl. Bio Mater.* **2018**, *1* (3), 581−592.

(8) Fesenmeier, D. J.; Suresh, M. V.; Kim, S.; Park, S.; Raghavendran, K.; Won, Y.-Y. Polymer Lung Surfactants Attenuate Direct Lung Injury in Mice. *ACS Biomater. Sci. Eng.* **2023**, *9* (5), 2716−2730.

(9) Barman, S.; Davidson, M. L.; Walker, L. M.; Anna, S. L.; Zasadzinski, J. A. Inflammation product effects on dilatational mechanics can trigger the Laplace instability and acute respiratory distress syndrome. *Soft Matter* **2020**, *16* (29), 6890−6901.

(10) Kim, S.; Fesenmeier, D. J.; Park, S.; Torregrosa-Allen, S. E.; Elzey, B. D.; Won, Y. Y. Pulmonary Pharmacokinetics of Polymer Lung Surfactants Following Pharyngeal Administration in Mice. *Biomacromolecules* **2022**, *23* (6), 2471−2484.

(11) Fesenmeier, D. J.; Kim, H. C.; Kim, S.; Won, Y.-Y. Determination of Block Copolymer Micelle Core T_g Using ^{1}H NMR Transverse (T_2) Relaxation Measurements of Micelle Coronas. *Macromolecules* **2023**, *56* (22), 9156−9163.

(12) Kim, S.; Park, S.; Fesenmeier, D. J.; Won, Y.-Y. Excipient-free lyophilization of block copolymer micelles for potential lung surfactant therapy applications. *Int. J. Pharm.* **2023**, *646*, 123476.

(13) Kim, S.; Park, S.; Fesenmeier, D. J.; Jun, T.; Sarkar, K.; Won, Y.-Y. Surface Pressure−Area Mechanics of Water-Spread Poly(ethylene glycol)-Based Block Copolymer Micelle Monolayers at the Air−Water Interface: Effect of Hydrophobic Block Chemistry. *Langmuir* **2023**, *39* (38), 13546−13559.

(14) Zuo, Y. Y.; Veldhuizen, R. A. W.; Neumann, A. W.; Petersen, N. O.; Possmayer, F. Current perspectives in pulmonary surfactant—Inhibition, enhancement and evaluation. *Biochim. Biophys. Acta, Biomembr.* **2008**, *1778* (10), 1947−1977.

(15) Zuo, Y. Y.; Keating, E.; Zhao, L.; Tadayyon, S. M.; Veldhuizen, R. A.; Petersen, N. O.; Possmayer, F. Atomic force microscopy studies of functional and dysfunctional pulmonary surfactant films. I. Micro-

and nanostructures of functional pulmonary surfactant films and the effect of SP-A. *Biophys. J.* **2008**, *94* (9), 3549−64.
(16) Alonso, C.; Alig, T.; Yoon, J.; Bringezu, F.; Warriner, H.; Zasadzinski, J. A. More than a monolayer: relating lung surfactant structure and mechanics to composition. *Biophys. J.* **2004**, *87* (6), 4188−202.
(17) Li, S.; Hanley, S.; Khan, I.; Varshney, S. K.; Eisenberg, A.; Lennox, R. B. Surface micelle formation at the air/water interface from nonionic diblock copolymers. *Langmuir* **1993**, *9* (8), 2243−2246.
(18) Zhang, L.; Eisenberg, A. Multiple Morphologies and Characteristics of "Crew-Cut" Micelle-like Aggregates of Polystyrene-*b*-Poly(acrylic acid) Diblock Copolymers in Aqueous Solutions. *J. Am. Chem. Soc.* **1996**, *118* (13), 3168−3181.
(19) Choucair, A.; Eisenberg, A. Control of amphiphilic block copolymer morphologies using solution conditions. *Eur. Phys. J. E* **2003**, *10* (1), 37−44.
(20) Yu, K.; Zhang, L.; Eisenberg, A. Novel Morphologies of "Crew-Cut" Aggregates of Amphiphilic Diblock Copolymers in Dilute Solution. *Langmuir* **1996**, *12* (25), 5980−5984.
(21) Fesenmeier, D. J.; Park, S.; Kim, S.; Won, Y.-Y. Surface mechanical behavior of water-spread poly(styrene)−poly(ethylene glycol) (PS−PEG) micelles at the air−water interface: Effect of micelle size and polymer end/linking group chemistry. *J. Colloid Interface Sci.* **2022**, *617*, 764−777.
(22) Zhulina, Y. B.; Birshtein, T. M. Conformations of block-copolymer molecules in selective solvents (micellar structures). *Polym. Sci. U.S.S.R.* **1985**, *27* (3), 570−578.
(23) Cao, B. H.; Kim, M. W. Molecular weight dependence of the surface tension of aqueous poly(ethylene oxide) solutions. *Faraday Discuss.* **1994**, *98* (0), 245−252.
(24) Zhang, H.; Fan, Q.; Wang, Y. E.; Neal, C. R.; Zuo, Y. Y. Comparative study of clinical pulmonary surfactants using atomic force microscopy. *Biochim. Biophys. Acta* **2011**, *1808* (7), 1832−42.
(25) Rubinstein, M.; Colby, R. H. *Polymer Physics*; Oxford University Press: New York, 2003; Vol. *23*.
(26) Fischer, V.; Borchard, W. Thermodynamic Properties of Poly(ethylene glycol)/Water Systems. 2. Critical Point Data. *J. Phys. Chem. B* **2000**, *104* (18), 4463−4470.
(27) Kumaki, J. Monolayer of polystyrene monomolecular particles on a water surface studied by Langmuir-type film balance and transmission electron microscopy. *Macromolecules* **1988**, *21* (3), 749−755.
(28) Fernsler, J. G.; Zasadzinski, J. A. Competitive adsorption: a physical model for lung surfactant inactivation. *Langmuir* **2009**, *25* (14), 8131−43.
(29) Fesenmeier, D J.; Kim, S.; Won, Y.-Y. Effect of Temperature on the Air-Water Surface Mechanical Behavior of Water-Spread Block Copolymer Micelles. *Soft Matter* **2023**, *19*, 9269−9281.
(30) Peltonen, J. P. K.; He, P.; Rosenholm, J. B. Order and defects of Langmuir-Blodgett films detected with the atomic force microscope. *J. Am. Chem. Soc.* **1992**, *114* (20), 7637−7642.

https://doi.org/10.1021/acsapm.4c00109
ACS Appl. Polym. Mater. 2024, 6, 2054−2060